

# Dispersive optical detection of magnetic Feshbach resonances in ultracold gases

Bianca J. Sawyer,<sup>1,\*</sup> Milena S.J. Horvath,<sup>1</sup> Eite Tiesinga,<sup>2</sup> Amita B. Deb,<sup>1</sup> and Niels Kjærgaard<sup>1,†</sup>

<sup>1</sup>*Department of Physics, QSO—Centre for Quantum Science, and Dodd-Walls Centre for Photonic & Quantum Technologies, University of Otago, Dunedin, New Zealand*

<sup>2</sup>*Joint Quantum Institute and Center for Quantum Information and Computer Science, National Institute of Standards and Technology and University of Maryland, Gaithersburg, Maryland 20899, USA*

(Dated: December 13, 2024)

Magnetically tunable Feshbach resonances in ultracold atomic systems are chiefly identified and characterized through time consuming atom loss spectroscopy. We describe an off-resonant dispersive optical probing technique to rapidly locate Feshbach resonances and demonstrate the method by locating four resonances of  $^{87}\text{Rb}$ , between the  $|F = 1, m_F = 1\rangle$  and  $|F = 2, m_F = 0\rangle$  states. Despite the loss features being  $\lesssim 0.1$  G wide, we require only 21 experimental runs to explore a magnetic field range  $> 18$  G, where  $1$  G =  $10^{-4}$  T. The resonances consist of two known *s*-wave features in the vicinity of 9 G and 18 G and two previously unreported *p*-wave features near 5 G and 10 G. We further utilize the dispersive approach to directly characterize the two-body loss dynamics for each Feshbach resonance.

Trapped ultracold gases have long been utilized as a highly controllable experimental testbed for the investigation of exciting and fundamental quantum phenomena such as matter wave interference [1], superfluidity [2] and the BEC-BCS crossover [3]. The standard technique for observing a cold atomic sample is time-of-flight absorption imaging where the entire sample is released from the trapping potential and illuminated with resonant laser light, projecting a shadow onto a charge coupled device (CCD) camera that gives the two-dimensional density distribution of the sample [4]. Conventional absorption imaging provides valuable information on the spatial distribution and internal quantum state of atoms. However, during the process the atoms are released from the confining potential and undergo a strong resonant interaction with the probe laser light, which heats up and destroys the sample. This allows for acquisition of just one data point per experimental run, and has motivated the development of probing methods using off-resonant light to reduce the spontaneous scattering rate of photons away from the probe beam, such as dispersive dark-ground imaging [5], phase contrast imaging [6, 7], and Faraday imaging [8–10].

For many applications the object of interest is not the spatial distribution of the cloud, but the temporal evolution of the atomic population within a given probing volume (an integral over the spatial distribution). For this class of measurements, a single photodiode would suffice for efficient data collection. This approach, in particular in conjunction with off-resonant probe light, has for example been used to monitor breathing [11] and spatial center-of-mass oscillations [12] of atomic samples, Rabi oscillations between hyperfine states [13–15], phase-space dynamics of spinor condensates [16] and Larmor precession [17]. While the spatial information imprinted on the probe laser beam is not retained, a photodiode provides an effective means for collecting high-bandwidth real-time temporal information during dynamical processes, for example, recording Rabi oscillations at a sample rate of  $\simeq 1$  MHz [18].

Feshbach resonances fall perfectly into the category of phenomena that can be efficiently explored through integrated dispersive measurements; the atom loss dynamics for a trapped gas driven by a Feshbach resonance is usually characterized via the total atom number, disregarding spatial information. The study of Feshbach resonances has remained an active field for more than two decades [19–21], in particular because it provides a powerful tool for tuning the scattering properties of atoms through external fields. Recent experiments include controlling the two-body Feshbach losses using electromagnetically induced transparency [22], investigation of *p*-wave Feshbach resonances in  $^6\text{Li}$  [23], and an interorbital Feshbach resonance in  $^{173}\text{Yb}$  [24]. There have also been recent proposals to produce Feshbach resonances using rf fields [25] and Rydberg molecular states [26].

In this paper we demonstrate the use of hyperfine state sensitive dispersive probing — measurement of the quantum state dependent phase shift acquired by an off-resonant probe beam as it passes through a sample — for efficiently locating and exploring the loss dynamics in connection to Feshbach resonances. In particular we consider  $^{87}\text{Rb}$ , which is one of the most prolifically utilized species in cold atom experiments worldwide, motivating the quest for a thorough understanding of its scattering properties, including details of its Feshbach landscape [27, 28]. We explore the magnetic field dependent collisional loss due to interactions between atoms in the  $5^2S_{1/2}|F = 1, m_F = 1\rangle \equiv |1, 1\rangle$  and  $5^2S_{1/2}|F = 2, m_F = 0\rangle \equiv |2, 0\rangle$  hyperfine substates, and identify four resonances in the range 0 G to 18 G [29, 30]. These consist of two previously observed *s*-wave features [31] as well as two *p*-wave features that have never been reported from prior experiments.

We begin the experiment by producing an ultracold sample of  $^{87}\text{Rb}$  atoms in the  $|F = 2, m_F = 2\rangle$  hyperfine Zeeman substate, using a standard laser-cooling apparatus [32]. We then transfer the sample from a magnetic trap into a double-well potential formed by two crossed-beam far-off-resonant dipole traps [33] and evaporatively cool to a temperature of  $1.4$   $\mu\text{K}$  by lowering the optical power of the horizontal confinement beam, as detailed in [34]. The sample now consists of two closely-spaced ellipsoidal atom clouds positioned along the  $z$ -axis. The double-well potential facilitates efficient loading of

\* [bianca.j.sawyer@postgrad.otago.ac.nz](mailto:bianca.j.sawyer@postgrad.otago.ac.nz)

† [nk@otago.ac.nz](mailto:nk@otago.ac.nz)

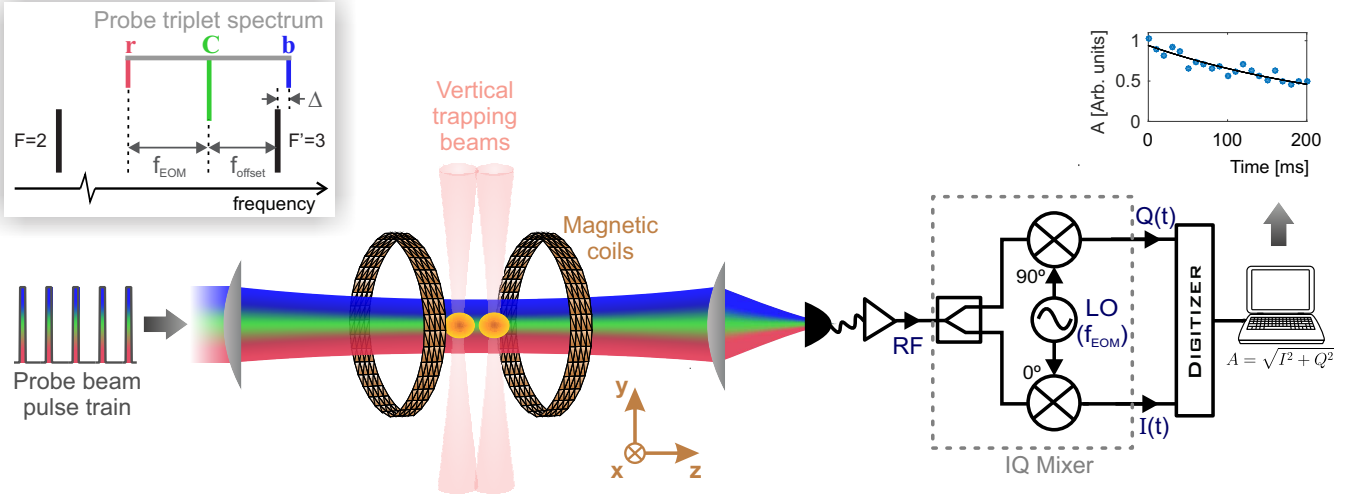


FIG. 1. (Color online) Schematic of the experimental setup, showing propagation of the pulsed trichromatic dispersive probing beam through the sample of optically-trapped  $^{87}\text{Rb}$ , followed by the demodulation electronics which extract phase shift information from the photo-detected signal. A typical post-processed data set and fit is shown in the plot to the far right. Note that the horizontal trapping beam, which completes the optical tweezer system, is co-propagating with the dispersive probe but is not shown here. Inset in upper left corner: the trichromatic frequency spectrum of the probe, consisting of a carrier (C), and red (r) and blue (b) sidebands. The probe is shown relative to the  $^{87}\text{Rb}$  ( $5^2\text{S}_{1/2}, F=2 \rightarrow 5^2\text{P}_{3/2}, F'=3$ ) absorption line (not to scale).

atoms from the elongated magnetic potential and provides the benefit of increased peak density over an elongated single-well potential, which increases the rate of Feshbach losses. Each well is characterized by axial and radial trapping frequencies  $(\omega_x, \omega_y, \omega_z) = 2\pi \times (243, 132, 156)$  Hz.

The magnetic field at the position of the atomic cloud is controlled by a coil pair arranged in the Helmholtz configuration, and points along the  $z$ -axis. This field,  $\mathbf{B} = B_z \hat{\mathbf{z}}$ , defines a quantization axis and lifts the degeneracy of the Zeeman sub-levels. Since the Feshbach resonances in  $^{87}\text{Rb}$  are narrow (all the known resonances are  $\lesssim 200$  mG wide), we use a current supply with  $10 \mu\text{A}/\text{A}$  stability to drive the Helmholtz coils. An arbitrary waveform generator controls the current supply, and the generated magnetic field has a stability better than 0.2 mG and has been calibrated using Rabi spectroscopy to an accuracy of  $\simeq 3$  mG. The experimental setup is summarized schematically in Fig. 1.

Using a sequence of microwave sweeps and pulses (see Supplemental Material [35], Sec. S.I) we prepare a sample of  $N \simeq 2.3 \times 10^6$  atoms at  $1.4 \mu\text{K}$  in a superposition of the  $|2,0\rangle$  and  $|1,1\rangle$  states. Before beginning our investigation of Feshbach dynamics we hold the sample in the trap for a further 12 ms, which exceeds the coherence time of the system, so the resulting sample can be treated as a 50–50 mixture of atoms in the  $|2,0\rangle$  and  $|1,1\rangle$  states, with a peak density of  $n_0 \simeq 2 \times 10^{19} \text{ m}^{-3}$  in each. We then sweep the magnetic field down linearly from a series of starting magnetic field values at a constant rate of  $-5.83 \text{ mG/ms}$ , with each sweep covering a range of 1.17 G over 200 ms. During the magnetic field sweep we monitor the dynamics of the atomic population in the  $|2,0\rangle$  state using an off-resonant dispersive probe beam. The probe beam is generated by an external cavity diode laser, locked at a red-detuned offset frequency  $f_{\text{offset}} = 3.30 \text{ GHz}$  from the  $F = 2 \rightarrow F' = 3$  transition of the D2 line, to within 4 MHz. By passing this carrier beam (C) through a fiber electro-optic

phase modulator we produce a trichromatic spectrum with 1<sup>st</sup>-order sidebands at  $\pm f_{\text{EOM}} = \pm 3.700 \text{ GHz}$ , where the carrier component has an optical power of  $\simeq 13 \mu\text{W}$  and each of the two first-order sidebands contain  $\simeq 1 \mu\text{W}$  (higher order sidebands have negligible power). The detuning of the blue sideband (b) is relatively small,  $\Delta = f_{\text{EOM}} - f_{\text{offset}} = +400 \text{ MHz}$ , while the red sideband (r) is  $-7.00 \text{ GHz}$  below the transition, and the resulting common-path interferometric probe triplet is illustrated schematically in the inset of Fig. 1. We note that the probing scheme is insensitive to atoms in the  $F = 1$  state, as the  $F = 1 \rightarrow F'$  transition is far-off-resonant for all probe triplet components.

During the 200 ms Feshbach field sweeps we probe the sample with a train of 21 light pulses at intervals of 10 ms. Each pulse has a duration of 600 ns and contains  $\simeq 3 \times 10^6$  photons in the probing (b) sideband. The pulsed probe beam propagates along the  $z$ -axis and is linearly polarized along the  $x$ -axis. We focus the probe beam to a  $28 \mu\text{m}$  waist and center it on the two ellipsoidal atomic clouds, which each have  $1/e$  Gaussian radii of  $(\sigma_x, \sigma_y, \sigma_z) = (11, 20, 17) \mu\text{m}$  at the beginning of the probe sequence.

As the probe triplet passes through the atomic sample, the blue frequency component acquires a phase shift dependent upon the  $|2,0\rangle$  population of the cloud. The beam is then focused onto a 4.2 GHz bandwidth fiber-coupled ac photodetector, where the three frequency components combine to produce a heterodyne signal at frequency  $f_{\text{EOM}}$ . Following an amplification stage, we use a passive IQ mixer to demodulate the signal to baseband and sample the output of each mixer port at a rate of  $20 \mu\text{s}^{-1}$  with a 16-bit digitizer. At the instance of each probe pulse, the digitized I and Q components are numerically integrated over and summed in quadrature to give the dispersive signal,  $A(t)$ , which is proportional to the  $|2,0\rangle$  population (an example processed data set is shown in Fig. 1).

Figure 2(a) presents the results of 21 magnetic field sweeps,

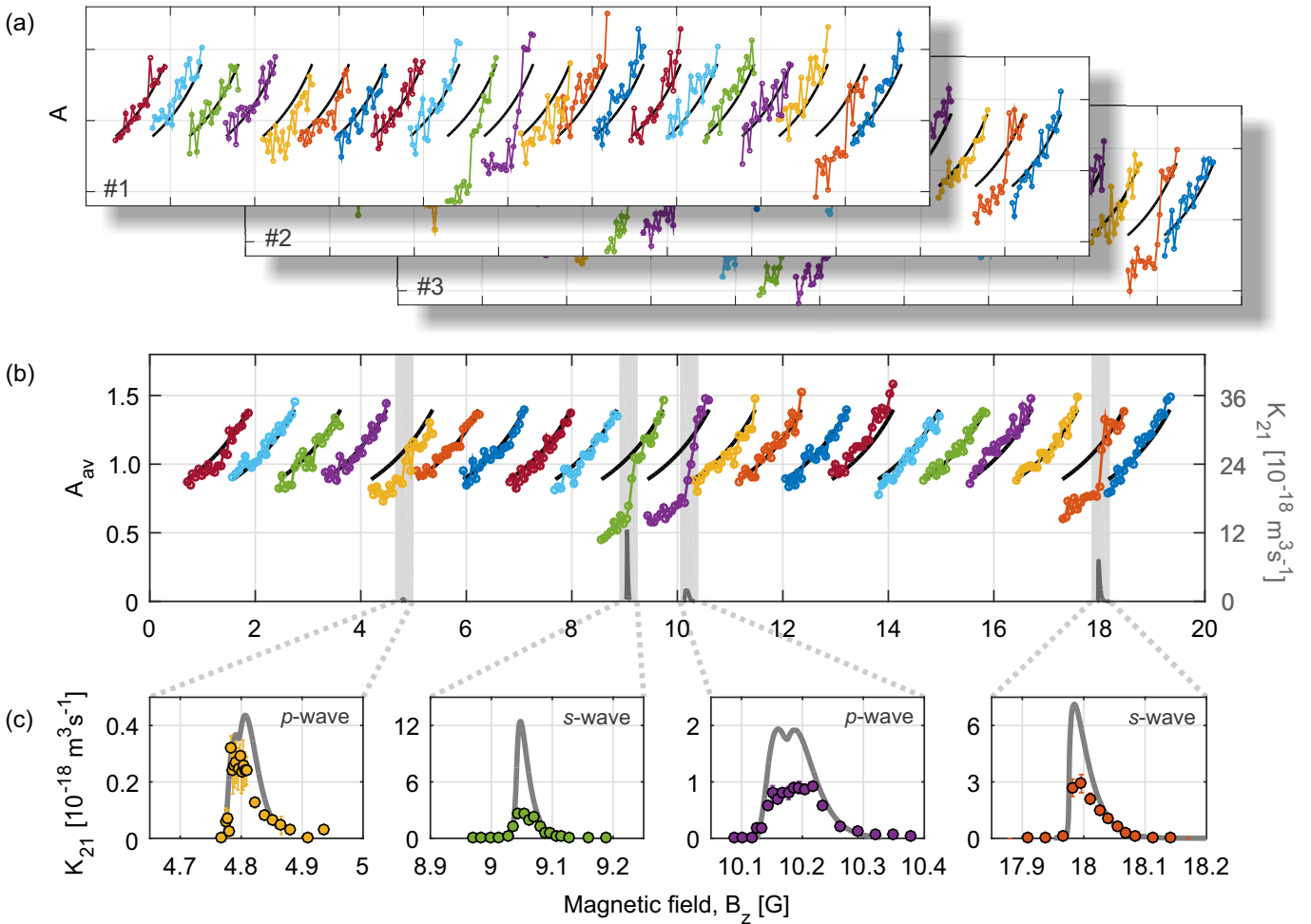


FIG. 2. (Color online) (a) Three data sets showing the single-experiment dispersive signal ( $A$ , arbitrary units) for 21 consecutive and overlapping magnetic field sweeps, covering the range 19.4 G – 0.7 G. The black line is a reference for comparison, as explained in Sec. S.II of the Supplemental Material [35]. (b) Left-hand axis: Dispersive signal averaged over the three experimental runs for each sweep,  $A_{av}$ . Right-hand axis: Theoretically predicted two-body loss rate coefficients ( $K_{21}$ , gray lines below dispersive data), calculated for a thermal ensemble of atoms at 1.4  $\mu$ K, about each of the four identified Feshbach resonances. (c) Zoomed-in view of the theoretically predicted  $K_{21}$  coefficients (gray lines), alongside the corresponding experimentally measured  $K_{21}$  coefficients (colored markers). One standard deviation uncertainties are indicated by error bars, which in most cases do not extend beyond the plotted point size.

which span a range from above 18 G to below 1 G and overlap by 25 % at each edge. The dispersive data set obtained for each sweep is plotted in sequence (colored circles) and superimposed on a reference trace (black line), derived from dispersive measurement of the background atom losses in a constant magnetic field  $B_z = 18.8$  G (see Supplemental Material [35], Sec. S.II). Four regions of interest, where the signal deviates from the reference, are shaded gray to indicate suspected Feshbach resonances. This is reinforced by Fig. 2(b), which shows the average of three repeated measurements for each magnetic field range. There are four clear steps in the signal, indicating Feshbach resonances at approximately 5 G, 9 G, 10 G and 18 G. By repeating the experiment about these four values with a pure sample of each component state ( $|2, 0\rangle$  and  $|1, 1\rangle$ ) separately, we verified that the Feshbach resonances observed all correspond to the mixed-spin entrance channel.

We further characterize the four observed Feshbach resonances by dispersively measuring the 2-body loss rate coeffi-

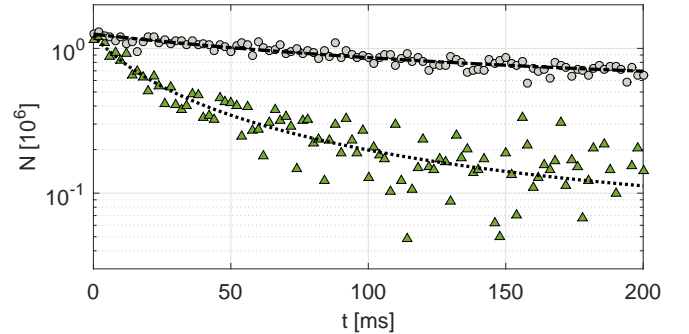


FIG. 3. (Color online) Atomic loss data acquired via dispersive probing as we hold the sample for 200 ms off-resonance (9.158 G, gray circles) and near-resonance (9.062 G, green triangles). Fits to the model described in the Supplemental Material [35], Sec. S.III are shown by a dash-dotted and dotted line, respectively.

cient,  $K_{21}$ , which describes the rate of enhanced losses near

a Feshbach resonance, as a function of magnetic field. We prepare the sample in the same way as above, but rather than sweeping the magnetic field, we hold it at a constant value for 200 ms while probing the  $|2,0\rangle$  component of the cloud dispersively with 600 ns pulses at intervals of 2 ms [36], hence following the evolution of atomic population in real time. The dispersive signal is converted to absolute atomic population  $N$  using a calibration based on absorption images (see Supplemental Material [35], Sec. S.III). In Fig. 3 we show example data sets for the atomic population decay at an on-resonance and an off-resonance magnetic field about the Feshbach resonance near 9 G. The off-resonant case displays an exponential decay, while the loss in the on-resonant case is much faster and non-exponential. Figure 3 also presents the result of fitting a nonlinear model to the data that captures both one- and two-body background losses and two-body Feshbach loss features (see Supplemental Material [35], Sec. S.III). The dispersive decay measurements are carried out in the vicinity of each resonance and values of the  $K_{21}$  coefficient are extracted from the fits to data, averaged over three data sets for each field value, and plotted in Fig. 2(c).

The theoretically predicted  $K_{21}$  coefficients for a thermal ensemble of atoms at 1.4  $\mu\text{K}$  are indicated by gray lines in Fig. 2(c). These are obtained from numerical coupled-channels calculations based on a Hamiltonian of a homonuclear pair of ground state  $^2\text{S}$   ${}^{87}\text{Rb}$  atoms with nuclear spin  $i = 3/2$  [37–39] that includes atomic hyperfine and Zeeman interactions, the isotropic  $\text{X}^1\Sigma_g^+$  and  $\text{a}^3\Sigma_u^+$  Born-Oppenheimer potentials, the centrifugal potential with partial wave  $\vec{\ell}$ , as well as the anisotropic electronic magnetic dipole-dipole and second-order spin-orbit interactions. Spectroscopically-accurate Born-Oppenheimer potentials and the parametrization of the second-order spin-orbit interaction are taken from Ref. [39]. The Hamiltonian conserves the sum of all spin and angular momentum projection quantum numbers and parity. Hence, even and odd partial waves remain uncoupled. As the two anisotropic interactions for  ${}^{87}\text{Rb}$  are weak it suffices to include all  $\ell = 0$  and 2 and  $\ell = 1$  and 3 channels for our  $s$ -wave and  $p$ -wave Feshbach resonances, respectively. Elastic and inelastic rate coefficients near the Feshbach resonances are first computed as a function of collision energy and then thermally averaged using energies up to ten times the temperature. Taking the resonance positions to be at the local maxima in the calculated  $K_{21}$  values, we get predicted  $s$ -wave peaks at 9.048 G and 17.985 G and  $p$ -wave doublets at {4.792 G, 4.806 G} and {10.160 G, 10.195 G}.

Agreement of the four experimentally determined resonance positions with theory is good and the expected qualitative characteristics are present in the data. There is a clear asymmetry in the  $K_{21}$  coefficient, with the tail trailing out toward higher values of magnetic field due to thermal broadening and there is also some evidence of the doublet structure of the  $p$ -wave Feshbach resonance near 10 G, which manifests due to the dipole-dipole interaction having different values depending on partial-wave projection,  $|m_l| = \{0, 1\}$  [40]. The  $K_{21}$  values shown in Fig. 2(c) are based on the assumption that the temperature is fixed at 1.4  $\mu\text{K}$  throughout the 200 ms

hold time, and for the resonance near 4.8 G, where the loss rate coefficient is small, we get good quantitative agreement with theory. For the other three resonances we get agreement in the wings, but the inferred  $K_{21}$  values are significantly lower than the theoretical predictions at the peak of each feature. We attribute this discrepancy to “anti-evaporative” heating of the sample [41], as Feshbach loss occurs preferentially from high density (low energy) regions of the sample, and the kinetic energy of the ejected atoms can be partially transferred to the thermal energy of the sample via collision with other particles during their escape [42].

To gain further insight into the effect of heating, we acquire an absorption image following the 200 ms hold time for each data set. From this it is apparent that larger Feshbach losses lead to a higher temperature increase, consistent with our finding of a larger discrepancy at the peak of the loss features. We find the predicted values of  $K_{21}$  to lie closer to a modeled  $K_{21}$  based on the final temperatures (for details see Supplemental Material [35], Sec. S.IV). While heating limits the applicability of our model to accurate measurement of large  $K_{21}$  values, it does not reduce the efficacy of the method for the purposes of detecting the locations of Feshbach resonances. A refined model, taking into account the time dependence of the temperature, would be better suited in order not to underestimate  $K_{21}$  at the peak.

We stress that to acquire equivalent information — for either the initial detection of Feshbach resonances or for characterization of their loss dynamics — using standard time-of-flight absorption imaging we would require a full experimental sequence ( $\approx 100$  s) per data point. In contrast, using dispersive probing we need just a single experimental run to monitor the evolution of atomic population over 200 ms, at a resolution of 2 ms. Other than the obvious benefit of saving time one-hundredfold, rapid data collection minimizes effects of drifting background fields and other experiment conditions, reducing sources of systematic error. We require 21 sweeps to cover the  $> 18$  G range at a rate slow enough to detect the weak resonance near 5 G, but for detection of stronger features it is possible to scan more rapidly, requiring fewer experimental runs to cover the same range (for an example see Supplemental Material [35], Sec. S.V).

In conclusion, we have demonstrated the use of an off-resonant heterodyne optical dispersive probing system to efficiently detect and characterize Feshbach resonances in ultracold  ${}^{87}\text{Rb}$ , and presented two previously unreported  $p$ -wave resonances. This provides a powerful new tool for mapping out the Feshbach resonances of any pair of substates, and fills a gap in the rich body of data on the widely used  ${}^{87}\text{Rb}$  species, but could straightforwardly be extended to any species with a change in optical frequencies, including those with optical Feshbach resonances [43]. Dispersive probing could be further utilized to investigate other types of loss dynamics near a Feshbach resonance, such as three-body losses and the associated Efimov signatures [44]. This will extend the applicability of the technique to broad resonances, where 2-body inelastic losses may be negligible over  $\approx 1$  s timescales. Finally, our method may provide an effective tool for the study of coherent atom-molecule oscillations in a BEC [45].

We thank Ryan Thomas for useful discussions.

- 
- [1] A. D. Cronin, J. Schmiedmayer, and D. E. Pritchard, *Rev. Mod. Phys.* **81**, 1051 (2009).
- [2] R. Desbuquois, L. Chomaz, T. Yefsah, J. Léonard, J. Beugnon, C. Weitenberg, and J. Dalibard, *Nat. Phys.* **8**, 645 (2012).
- [3] M. Randeria and E. Taylor, *Annu. Rev. Condens. Matter Phys.* **5**, 209 (2014).
- [4] W. Ketterle, D. S. Durfee, and D. M. Stamper-Kurn, in *Bose-Einstein Condensation in Atomic Gases, Proceedings of the International School of Physics "Enrico Fermi"*, Vol. 140, edited by M. Inguscio, S. Stringari, and C. E. Wieman (IOS Press, Amsterdam, 1999) pp. 67–176.
- [5] M. R. Andrews, M.-O. Mewes, N. J. van Druten, D. S. Durfee, D. M. Kurn, and W. Ketterle, *Science* **273**, 84 (1996).
- [6] M. R. Andrews, D. M. Kurn, H.-J. Miesner, D. S. Durfee, C. G. Townsend, S. Inouye, and W. Ketterle, *Phys. Rev. Lett.* **79**, 553 (1997).
- [7] P. B. Wigley, P. J. Everitt, K. S. Hardman, M. R. Hush, C. H. Wei, M. A. Sooriyabandara, P. Manju, J. D. Close, N. P. Robins, and C. C. N. Kuhn, *Optics Letters* **41**, 4795 (2016).
- [8] F. Kaminski, N. S. Kampel, M. P. H. Steenstrup, A. Griesmaier, E. S. Polzik, and J. H. Müller, *Eur. Phys. J. D* **66**, 227 (2012).
- [9] M. Gajdacz, P. L. Pedersen, T. Mørch, A. J. Hilliard, J. Arlt, and J. F. Sherson, *Rev. Sci. Instrum.* **84**, 083105 (2013).
- [10] M. Gajdacz, A. J. Hilliard, M. A. Kristensen, P. L. Pedersen, C. Klempt, J. J. Arlt, and J. F. Sherson, *Phys. Rev. Lett.* **117**, 073604 (2016).
- [11] P. G. Petrov, D. Oblak, C. L. G. Alzar, N. Kjærgaard, and E. S. Polzik, *Phys. Rev. A* **75**, 033803 (2007).
- [12] M. Kohnen, P. G. Petrov, R. A. Nyman, and E. A. Hinds, *New J. Phys.* **13**, 085006 (2011).
- [13] S. Chaudhury, G. A. Smith, K. Schulz, and P. S. Jessen, *Phys. Rev. Lett.* **96**, 043001 (2006).
- [14] S. Bernon, T. Vanderbrugge, R. Kohlhaas, A. Bertoldi, A. Landragin, and P. Bouyer, *New J. Phys.* **13**, 065021 (2011).
- [15] A. Deb, B. Sawyer, and N. Kjærgaard, *Phys. Rev. A* **88**, 063607 (2013).
- [16] Y. Liu, E. Gomez, S. Maxwell, L. Turner, E. Tiesinga, and P. D. Lett, *Phys. Rev. Lett.* **102**, 225301 (2009).
- [17] T. Isayama, Y. Takahashi, N. Tanaka, K. Toyoda, K. Ishikawa, and T. Yabuzaki, *Phys. Rev. A* **59**, 4836 (1999).
- [18] P. J. Windpassinger, D. Oblak, P. G. Petrov, M. Kubasik, M. Saffman, C. L. G. Alzar, J. Appel, J. H. Müller, N. Kjærgaard, and E. S. Polzik, *Phys. Rev. Lett.* **100**, 103601 (2008).
- [19] E. Tiesinga, A. J. Moerdijk, B. J. Verhaar, and H. T. C. Stoof, *Phys. Rev. A* **46**, R1167 (1992).
- [20] S. Inouye, M. R. Andrews, J. Stenger, H.-J. Miesner, D. M. Stamper-Kurn, and W. Ketterle, *Nature* **392**, 151 (1998).
- [21] T. Maier, H. Kadau, M. Schmitt, M. Wenzel, I. Ferrier-Barbut, T. Pfau, A. Frisch, S. Baier, K. Aikawa, L. Chomaz, and et al., *Physical Review X* **5**, 041029 (2015).
- [22] A. Jagannathan, N. Arunkumar, J. A. Joseph, and J. E. Thomas, *Phys. Rev. Lett.* **116**, 075301 (2016).
- [23] T. Nakasuij, J. Yoshida, and T. Mukaiyama, *Phys. Rev. A* **88**, 012710 (2013).
- [24] M. Höfer, L. Rieger, F. Scazza, C. Hofrichter, D. R. Fernandes, M. M. Parish, J. Levinsen, I. Bloch, and S. Fölling, *Phys. Rev. Lett.* **115**, 265302 (2015).
- [25] D. J. Owens, T. Xie, and J. M. Hutson, *Phys. Rev. A* **94**, 023619 (2016).
- [26] N. Sándor, R. González-Férez, P. S. Julienne, and G. Pupillo, *arXiv preprint arXiv:1611.07091* (2016).
- [27] S. Tojo, Y. Taguchi, Y. Masuyama, T. Hayashi, H. Saito, and T. Hirano, *Phys. Rev. A* **82**, 033609 (2010).
- [28] C. A. Regal, C. Ticknor, J. L. Bohn, and D. S. Jin, *Phys. Rev. Lett.* **90**, 053201 (2003).
- [29] Units of gauss rather than tesla (the accepted SI unit for the magnetic field) have been used in this paper, as is conventional in this field of physics. The conversion is 1 G =  $10^{-4}$  T.
- [30] M. S. Horvath, R. Thomas, E. Tiesinga, A. B. Deb, and N. Kjærgaard, *arXiv preprint arXiv:1704.07109* (2017).
- [31] A. M. Kaufman, R. P. Anderson, T. M. Hanna, E. Tiesinga, P. S. Julienne, and D. S. Hall, *Phys. Rev. A* **80**, 050701 (2009).
- [32] B. J. Sawyer, A. B. Deb, T. McKellar, and N. Kjærgaard, *Phys. Rev. A* **86**, 065401 (2012).
- [33] K. O. Roberts, T. McKellar, J. Fekete, A. Rakonjac, A. B. Deb, and N. Kjærgaard, *Opt. Lett.* **39**, 2012 (2014).
- [34] A. B. Deb, T. McKellar, and N. Kjærgaard, *Phys. Rev. A* **90**, 051401 (2014).
- [35] See Supplemental Material for details of the state preparation, reference trace, population decay model, effect of heating and an alternative set of field sweeps.
- [36] For the data about the 18 G resonance, the probing interval is 5 ms. This does not result in any differences in the analysis of the data, but gives data of lower resolution.
- [37] H. T. C. Stoof, J. M. V. A. Koelman, and B. J. Verhaar, *Phys. Rev. B* **38**, 4688 (1988).
- [38] P. J. Leo, C. J. Williams, and P. S. Julienne, *Phys. Rev. Lett.* **85**, 2721 (2000).
- [39] C. Strauss, T. Takekoshi, F. Lang, K. Winkler, R. Grimm, J. Hecker Denschlag, and E. Tiemann, *Phys. Rev. A* **82**, 052514 (2010).
- [40] C. Ticknor, C. A. Regal, D. S. Jin, and J. L. Bohn, *Phys. Rev. A* **69**, 042712 (2004).
- [41] U. Eismann, L. Khaykovich, S. Laurent, I. Ferrier-Barbut, B. S. Rem, A. T. Grier, M. Delehaye, F. Chevy, C. Salomon, L.-C. Ha, and C. Chin, *Phys. Rev. X* **6**, 021025 (2016).
- [42] C. Regal and D. Jin, in *Advances In Atomic, Molecular, and Optical Physics*, Vol. 54, edited by C. L. P.R. Berman and E. Arimondo (Elsevier, 2007) pp. 1–79.
- [43] S. Blatt, T. L. Nicholson, B. J. Bloom, J. R. Williams, J. W. Thomsen, P. S. Julienne, and J. Ye, *Phys. Rev. Lett.* **107**, 073202 (2011).
- [44] F. Ferlaino, A. Zenesini, M. Berninger, B. Huang, H. C. Nägerl, and R. Grimm, *Few-Body Systems* **51**, 113 (2011).
- [45] E. A. Donley, N. R. Claussen, S. T. Thompson, and C. E. Wieman, *Nature* **417**, 529 (2002).

## Supplemental Material for:

### Dispersive optical detection of magnetic Feshbach resonances in ultracold gases

Bianca J. Sawyer<sup>1</sup>, Milena S.J. Horvath<sup>1</sup>, Eite Tiesinga<sup>2</sup>, Amita B. Deb<sup>1</sup>, and Niels Kjærgaard<sup>1</sup>

<sup>1</sup> Department of Physics, QSO—Centre for Quantum Science, and Dodd-Walls Centre for Photonic & Quantum Technologies, University of Otago, Dunedin, New Zealand

<sup>2</sup> Joint Quantum Institute and Center for Quantum Information and Computer Science, National Institute of Standards and Technology and University of Maryland, Gaithersburg, Maryland 20899, USA

#### S.I. STATE PREPARATION

We convert our  $|2, 2\rangle$  ultracold  $^{87}\text{Rb}$  sample into a nearly 50-50 mixture of the  $|2, 0\rangle$  and  $|1, 1\rangle$  quantum states using microwave-frequency transitions, following loading into the crossed-beam dipole trap. First, we use a frequency sweep across the  $|2, 2\rangle \leftrightarrow |1, 1\rangle$  resonance to transfer the population by adiabatic rapid passage (ARP) [S1] to  $|1, 1\rangle$ , in the presence of a small homogeneous bias field  $B_z = 2.0$  G. We ensure purity of our sample by removing any atoms remaining in the  $F = 2$  multiplet with a 1 ms optical clearing pulse, resonant with the  $\{5^2S_{1/2}, F = 2\} \rightarrow \{5^2P_{3/2}, F' = 3\}$  optical transition. The field is then ramped up to 18.8 G over 10 ms and a  $\pi/2$ -pulse, resonant with the  $|1, 1\rangle \rightarrow |2, 0\rangle$  transition, is used to prepare the sample in a superposition of the  $|2, 0\rangle$  and  $|1, 1\rangle$  states. A typical magnetic field profile over the course of our experiment is shown schematically in Fig. S1, indicating the two state preparation stages and the magnetic field ramp used to scan for Feshbach resonances.

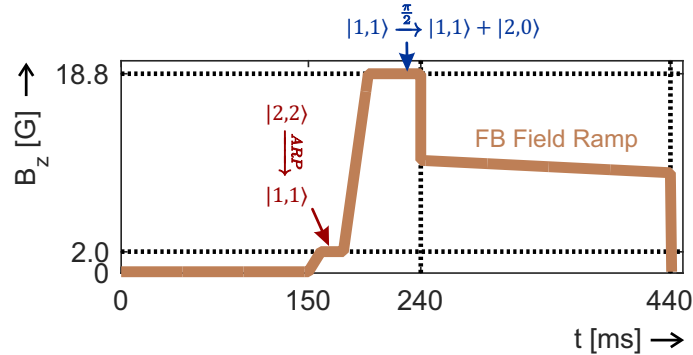


FIG. S1. (Color online) Typical magnetic field profile during an experimental run, indicating the timing of the two state preparation stages; adiabatic rapid passage (ARP) and a resonant  $\pi/2$ -pulse ( $\frac{\pi}{2}$ ).

The state preparation sequence for the measurement of  $K_{21}$  loss rate coefficients is almost identical to that above, but with one subtle difference. Because we need high magnetic field stability to precisely characterize narrow loss features, we carry out the  $\pi/2$ -pulse at a magnetic field  $< 2$  G above the resonance of interest (at 18.8 G, 10.9 G, 10.9 G and 5.4 G for each resonance respectively). This minimizes ringing of the field when we decrease it to a fixed field value near resonance during the  $K_{21}$  investigations, while avoiding atom loss due to Feshbach dynamics during the state preparation.

#### S.II. REFERENCE TRACE FOR MAGNETIC FIELD SWEEPS

To determine whether a decrease in the dispersive signal acquired during a magnetic field sweep is indicative of a Feshbach resonance, we acquire a reference signal in the presence of a constant off-resonance magnetic field ( $B_z = 18.8$  G). This reference signal, averaged over three runs, is shown in Fig. S2 (gray circles) alongside a fit to the model in Sec. S.III, with the  $K_{21}$  loss rate coefficient set to zero. This fitted line is plotted in 2(b) of the main text (solid black lines) with the time axis recalibrated to match each of the 21 magnetic field sweeps, for easy comparison of the two signals.

#### S.III. MODEL FOR DECAY DATA AND DISPERSIVE SIGNAL

In this section we derive a model for the time evolution of a trapped sample population held in a constant magnetic field. We then relate this to the measured dispersive signal, from which we extract the parameters describing the loss dynamics near a Feshbach resonance.

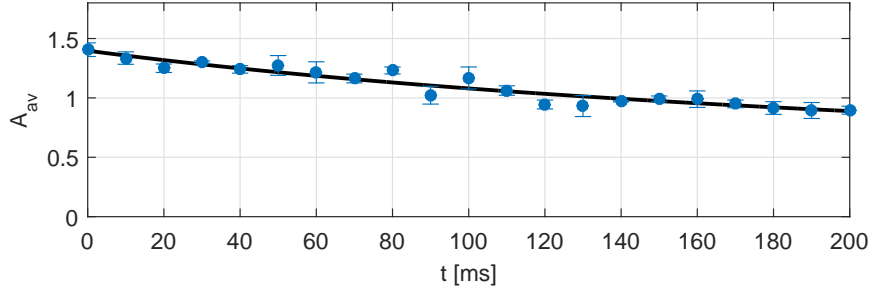


FIG. S2. (Color online) Reference dispersive signal, acquired at constant off-resonance magnetic field (blue circles), and a fit to the model presented in Sec. S.III (solid black line). Error bars represent uncertainties of one standard deviation.

The crossed-beam dipole-trapped  $|1,1\rangle$  and  $|2,0\rangle$  state populations,  $N_1(t)$  and  $N_2(t)$ , respectively, are modeled by a pair of coupled rate equations

$$\frac{dn_1(\mathbf{r},t)}{dt} = -\Gamma_1 n_1(\mathbf{r},t) - 2K_{11} n_1(\mathbf{r},t)^2 - K_{21} n_1(\mathbf{r},t) n_2(\mathbf{r},t), \quad (\text{S1})$$

and

$$\frac{dn_2(\mathbf{r},t)}{dt} = -\Gamma_2 n_2(\mathbf{r},t) - 2K_{22} n_2(\mathbf{r},t)^2 - K_{21} n_2(\mathbf{r},t) n_1(\mathbf{r},t), \quad (\text{S2})$$

where  $n_1(\mathbf{r},t)$  and  $n_2(\mathbf{r},t)$  are the atomic densities of the populations at time  $t$  and position  $\mathbf{r}$  in the crossed-beam dipole trap,  $\Gamma_1$  and  $\Gamma_2$  are the one-body loss rates due to collisions with molecules or atoms in the background vacuum, and  $K_{11}$ ,  $K_{22}$  and  $K_{21}$  are the thermally-averaged two-body loss rate coefficients for  $\{1,1+1,1\}$ ,  $\{2,0+2,0\}$  and  $\{2,0+1,1\}$  interactions, respectively [S2, S3] (we exclude three-body recombination processes, which we estimate to be negligible in our system). The factor of two preceding the  $K_{11}$  and  $K_{22}$  terms in Eq. S1 and Eq. S2 arises because each collision event leads to the loss of two  $|1,1\rangle$  or two  $|2,0\rangle$  atoms, respectively, rather than one of each as in the  $K_{21}$  process.

For a 3D Gaussian density profile with width  $(\sigma_x, \sigma_y, \sigma_z)$ , Eq. S1 and Eq. S2 can be integrated over space to give the rate equations for the crossed-beam dipole-trapped sample populations,

$$\frac{dN_1(t)}{dt} = -\Gamma_1 N_1(t) - \frac{2K_{11}}{(2\pi)^{3/2}\sigma_x\sigma_y\sigma_z} N_1(t)^2 - \frac{K_{21}}{(2\pi)^{3/2}\sigma_x\sigma_y\sigma_z} N_1(t) N_2(t), \quad (\text{S3})$$

and

$$\frac{dN_2(t)}{dt} = -\Gamma_2 N_2(t) - \frac{2K_{22}}{(2\pi)^{3/2}\sigma_x\sigma_y\sigma_z} N_2(t)^2 - \frac{K_{21}}{(2\pi)^{3/2}\sigma_x\sigma_y\sigma_z} N_2(t) N_1(t). \quad (\text{S4})$$

The cloud widths are temperature dependent, with the relationship given by

$$\sigma_i = \sqrt{\frac{2 k_B T}{m}} \frac{1}{\omega_i}, \quad (\text{S5})$$

where  $i = x, y, z$ ,  $k_B$  is the Boltzmann constant,  $T$  the temperature of the atoms in the crossed-beam dipole trap,  $m$  the mass of a  $^{87}\text{Rb}$  atom and  $\omega_i$  the trapping frequency of the dipole trap along direction  $i$ .

Our dispersive probe measurement scheme is sensitive to atoms in the  $F = 2$  ground-state hyperfine manifold, and produces a signal proportional to the  $|2,0\rangle$  state population. The dispersive probe beam causes a small perturbation to the  $|2,0\rangle$  component of our sample; a series of 101 dispersive pulses typically results in a 10 % temperature increase and a 20 % population decrease for the experiments in this work. It appears that the affected atoms are pushed out of the crossed-trap potential but remain trapped by the horizontal waveguide beam, and a second population of  $|2,0\rangle$  atoms,  $N_2^W$ , accumulates. A schematic of the two trapped populations and their associated loss rate coefficients is shown in Fig. S3. Because the horizontal waveguide beam propagates coaxially with the dispersive probe beam, both the  $N_2$  and the  $N_2^W$  populations contribute to the dispersive signal

$$A = (C_2 N_2 + C_2^W N_2^W) + A_0, \quad (\text{S6})$$

where  $A_0$  is an offset and  $C_2$  and  $C_2^W$  are calibration constants, determined by comparing dispersive signal amplitudes to the corresponding atom numbers measured using absorption imaging at a temperature of  $T = 1.4 \mu\text{K}$  (we assume  $C_2 = C_2^W$ ).

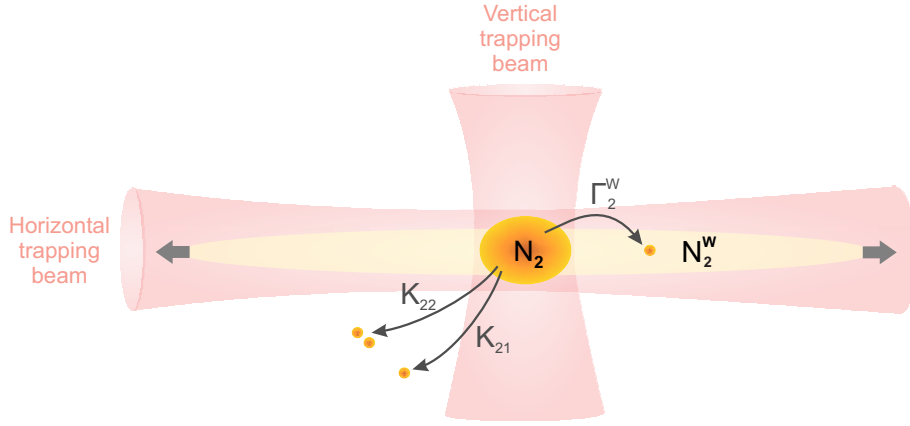


FIG. S3. (Color online) Schematic of the two distinct  $|2,0\rangle$  populations that contribute to the dispersive signal.  $N_2$  atoms are confined by the crossed-beam dipole trap, while  $N_2^W$  atoms are confined by the horizontally-propagating trapping potential only, and arrows at each end indicate continued expansion along this waveguide beam.  $\Gamma_2^W$  is the rate of atom removal from population  $N_2$  to population  $N_2^W$ , and  $K_{22}$  and  $K_{21}$  are the two-body losses from population  $N_2$  to the background vacuum. Note that the density of the waveguide population is much lower than that of the sample, so two-body losses are negligible.

To describe the effect of the dispersive probe beam on our system we require a third rate equation,

$$\frac{dN_2^W}{dt} = +\Gamma_2^W N_2 - \Gamma_2 N_2^W, \quad (S7)$$

where  $\Gamma_2^W$  is the rate at which  $|2,0\rangle$  atoms move from the crossed-dipole trap into the horizontal waveguide due to interaction with the dispersive probe beam, and we replace  $\Gamma_2$  with  $\Gamma_2 + \Gamma_2^W$  in Eq. S4. The dispersive probe does not lead to additional  $|1,1\rangle$  atom losses, as the  $|1,1\rangle$  state is unaffected by the probe. Two-body losses from the  $N_2^W$  population are negligible over the timescale of our experiment, as the atomic density is very low. From a series of dispersive probe measurements with varying pulse number we have measured a loss rate per probe pulse of  $0.011 \text{ s}^{-1}$ , so for a sequence of 101 pulses,  $\Gamma_2^W = 1.1 \text{ s}^{-1}$ .

#### Fitting background data

We consider our reference data sets, where the magnetic field is held constant at an off-resonant value  $\sim 1 \text{ G}$  above the Feshbach resonance, and use Eq. S6 to convert the dispersive signal into total  $|2,0\rangle$  state population. We then fit a model for the temporal evolution of  $|2,0\rangle$  atom number in the absence of two-body Feshbach losses, which is given by the sum of the two  $|2,0\rangle$  populations

$$N_{\text{tot}}(t) = N_2(t) + N_2^W(t), \quad (S8)$$

where the two respective populations are given by the solution to the system of three coupled differential equations

$$\frac{dN_2(t)}{dt} = -\Gamma_2^W N_2(t) - \frac{2K_{22}}{(2\pi)^{3/2}\sigma_x\sigma_y\sigma_z} N_2(t)^2 - \frac{K_{21}}{(2\pi)^{3/2}\sigma_x\sigma_y\sigma_z} N_2(t)N_1(t), \quad (S9)$$

$$\frac{dN_1(t)}{dt} = -\frac{K_{21}}{(2\pi)^{3/2}\sigma_x\sigma_y\sigma_z} N_1(t)N_2(t), \quad (S10)$$

and

$$\frac{dN_2^W}{dt} = +\Gamma_2^W N_2, \quad (S11)$$

with initial conditions  $N_2(t=0) = N_1(t=0) = N_0$  and  $N_2^W(t=0) = 0$ . In deriving this system of equations, we made use of the fact that  $(\Gamma_1, \Gamma_2, K_{11}n_0) \ll (K_{21}n_0, K_{22}n_0)$  for typical values of  $n_0$  (the initial single-component peak atomic density) to neglect the terms involving  $\Gamma_1, \Gamma_2$  and  $K_{11}$  in Eq. S3, Eq. S4 and Eq. S7. To fit to the off-resonant data sets we set  $K_{21} = 0$  and used  $N_0$  and  $K_{22}$  as our fitting parameters. For each of the four data series,  $K_{22} \simeq 1.0 \times 10^{-19} \text{ m}^3 \text{s}^{-1}$  (or equivalently,  $K_{22}n_0 \simeq 2.0 \text{ s}^{-1}$ ).

### Fitting Feshbach loss data

Using the values of  $K_{22}$  obtained from our off-resonant data sets, we then fitted our near-resonance data sets with Eq. S8 and fitting parameters  $N_0$  and  $K_{21}$ . The extracted values of the two-body loss rate coefficients  $K_{21}$  for each magnetic field value are shown in Fig. 2(c) of the main text. The maximum two-body peak loss rate of  $K_{21}n_0 \simeq 60 \text{ s}^{-1}$  was measured for the  $\simeq 18 \text{ G}$  resonance. Fitting to a simpler model where the losses into the waveguide are neglected (i.e. setting  $\Gamma_2^W = 0$ ) gives a very similar result, with the extracted  $K_{21}$  loss rate coefficients  $\leq 10 \%$  smaller in magnitude.

### S.IV. INVESTIGATION OF HEATING DURING LOSS MEASUREMENTS

We acquired a time-of-flight absorption image immediately following every dispersive measurement. From the images we extracted the spatial distribution of the crossed-beam dipole-trapped  $|2,0\rangle$  component following 200 ms of dispersive probing at fixed magnetic field, and calculated the final population and temperature. The measured final  $|2,0\rangle$  population in the crossed-trap versus magnetic field is presented in the top row of Fig. S4 and amounts to a set of traditional loss spectroscopy measurements. The resonance positions and qualitative shape of the loss features match with those in Fig. 2(c) of the main text, which verifies the validity of our method for analyzing dispersively measured loss dynamics. The measured final temperature versus magnetic field is presented in the bottom row of Fig. S4, and shows that the temperature of the cloud increases as a result of loss dynamics in the vicinity of a Feshbach resonance. The resonance positions and qualitative shape of the loss features are also mimicked in the temperature data, and we even see the expected doublet-structure near 10 G.

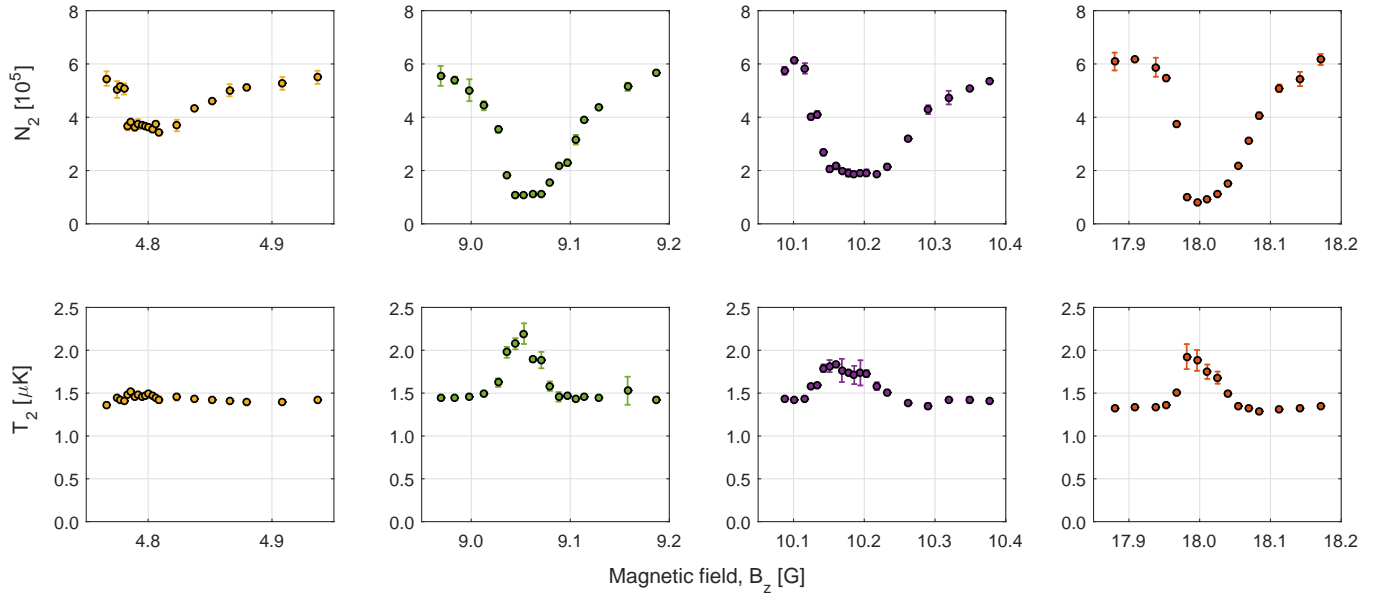


FIG. S4. (Color online) Dipole trapped  $|2,0\rangle$  population (top row) and temperature (bottom row) derived from time-of-flight absorption images, following a 200 ms hold time at a range of magnetic fields across four Feshbach resonances. One standard deviation uncertainties are indicated by error bars, which in most cases do not extend beyond the plotted point size.

### Relationship between the decay model and temperature

In deriving the rate equations for the atomic populations, Eq. S10, Eq. S9 and Eq. S11, we assumed that the sample had a thermal Gaussian distribution of fixed temperature [S3], and hence that the sample size was constant throughout the loss process. Because the sample heats up during Feshbach interactions it expands according to Eq. S5, and the model presented in Sec. S.III underestimates the  $K_{21}$  loss rate coefficients near resonance. Ideally we need an extended model with time-dependent cloud size  $\{\sigma_x(T(t)), \sigma_y(T(t)), \sigma_z(T(t))\}$  to account for the effect of the heating. This would require an understanding of how temperature changes with time, which is not straightforward because heating is correlated with the  $K_{21}$  coefficient. While this extension falls outside the scope of our current work, Fig. S5 shows the  $K_{21}$  values recalculated using the final temperature for each data set in the model detailed in Sec. S.III (red triangles), rather than the initial temperature of  $1.4 \mu\text{K}$  (also shown for reference, with

colored circles). A solid gray line shows the theoretical  $K_{21}$  values for an ensemble at  $1.4 \mu\text{K}$ , while the dotted black line is the theoretical curve for an ensemble at temperatures of  $1.6 \mu\text{K}$ ,  $2.3 \mu\text{K}$ ,  $1.9 \mu\text{K}$  and  $2.0 \mu\text{K}$ , which are the maximum temperatures observed following Feshbach loss about the resonances near 5 G, 9 G, 10 G and 18 G, respectively.

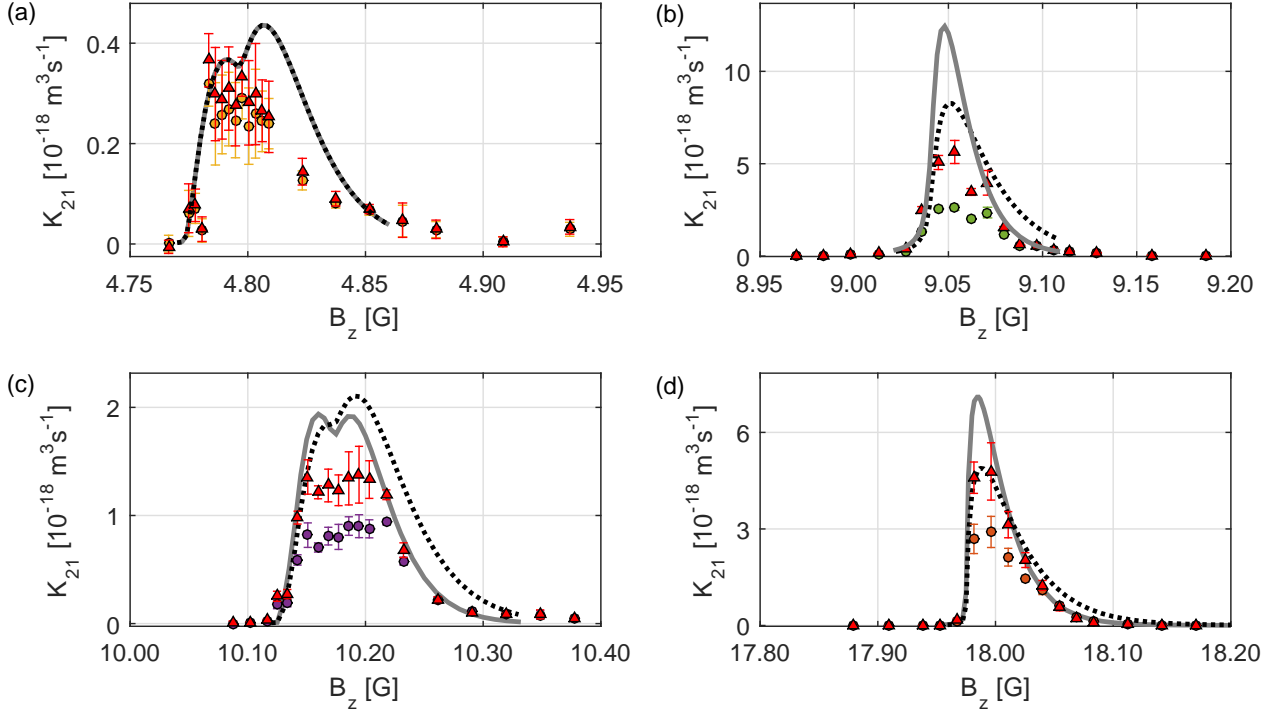


FIG. S5. (Color online) Two-body loss rate coefficient,  $K_{21}$ , for the four identified Feshbach resonances. Colored circles indicate the measured values as in Fig. 2(c), and red triangles indicate the measured values based on the expected cloud size at the measured final ensemble temperatures for each data point. In each panel the solid gray line shows the theoretical curve for an ensemble at  $1.4 \mu\text{K}$  while the dotted black line is the theoretical curve for an ensemble at temperatures of  $1.6 \mu\text{K}$ ,  $2.3 \mu\text{K}$ ,  $1.9 \mu\text{K}$  and  $2.0 \mu\text{K}$  for the resonances in panels a-d respectively. Note that the two curves overlap in the  $\simeq 5 \text{ G}$  case.

For data points where the temperature increase during the 200 ms hold time was small, we expect the dispersively measured  $K_{21}$  values to match closely with the  $1.4 \mu\text{K}$  (gray solid) theory curve. This is the case in the wings of the 9 G, 10 G and 18 G features, and at most magnetic fields about the 5 G feature, as can be seen in Fig. S5. On the other hand, we expect the dispersively measured  $K_{21}$  values to match more closely with the variable upper temperature limit (black dotted) theory curve where the heating effect was significant, and see evidence of this behavior toward the peaks of the three higher-field features. The effect of heating may also explain why the doublet structure of the 10 G  $p$ -wave resonances is not clear — it has been washed out due to thermal broadening [S4], the effect of which we can also see in the corresponding theoretical curve for a thermal sample at  $1.9 \mu\text{K}$ . While modifying the temperature used in our model gives values of  $K_{21}$  that match more closely with the theory, there is still a discrepancy between experiment and theory in all but the  $\simeq 18 \text{ G}$  case.

#### Relationship between dispersive signal and temperature

The coupling factor  $C_2$ , entering the expression in Eq. S6 that relates the dispersive signal to the atomic population, depends on the geometry of both the atomic sample and the dispersive probe beam. In our experiments the dispersive probe beam parameters remain fixed, but the temperature increases slightly during Feshbach interactions, increasing the ensemble size according to Eq. S5. Because the temporal evolution of the temperature during these processes is unknown, we assumed a fixed coupling factor (measured at  $T = 1.4 \mu\text{K}$ ) to convert dispersive signal to atomic population.

The Rayleigh range of our dispersive beam is  $z_R \simeq 3 \text{ mm} \gg \sigma_z \simeq 17 \mu\text{m}$ , so we ignore intensity variations along the direction of propagation and consider only the Gaussian intensity profile in the radial (xy) plane,

$$I(x, y) = I_0 e^{-\frac{2x^2 + 2y^2}{w_0^2}}, \quad (\text{S12})$$

where  $I_0$  is the peak intensity and  $w_0 = 28 \mu\text{m}$  is the beam waist. Assuming our sample is at thermal equilibrium, the spatial

profile of atoms can be well-approximated by a 2D Gaussian column density distribution

$$n(x, y) = 2\sqrt{\pi}\sigma_z n_0 e^{-\left(\frac{x^2}{\sigma_x^2} + \frac{y^2}{\sigma_y^2}\right)}, \quad (\text{S13})$$

where the factor of two arises from the fact that our sample consists of two identical Gaussian clouds in series along the direction of propagation, and  $n_0$  is the peak atomic density

$$n_0 = \frac{N_2}{\sigma_x \sigma_y \sigma_z (2\pi)^{3/2}}. \quad (\text{S14})$$

The dispersive signal ( $A$ ) can be expressed as

$$A = k \int_{-\infty}^{\infty} \int_{-\infty}^{\infty} n(x, y) I(x, y) dx dy, \quad (\text{S15})$$

where  $k$  is a fixed constant of proportionality that depends on the electronic system used to demodulate the signal, the resonant optical cross section, and the detuning of the probe light from resonance. Evaluating this integral gives

$$A = 2k\pi^{3/2} I_0 n_0 \frac{w_0^2 \sigma_x \sigma_y \sigma_z}{(2\sigma_x^2 + w_0^2)^{1/2} (2\sigma_y^2 + w_0^2)^{1/2}}. \quad (\text{S16})$$

To determine the dependence of the coupling factor on the temperature ( $T$ ) and the atomic population ( $N_2$ ), we substitute in Eq. S5 and Eq. S14 to give

$$A(T) = \frac{kI_0}{\sqrt{2}} \frac{w_0^2}{\left(w_0^2 + \frac{4k_B T}{m\omega_x^2}\right)^{1/2} \left(w_0^2 + \frac{4k_B T}{m\omega_y^2}\right)^{1/2}} N_2 = C_2(T) N_2 \quad (\text{S17})$$

Figure S6 shows the variation in the coupling factor over the full range of temperatures we observe, normalized to the value of the coupling factor at the initial temperature. The dotted lines indicate the maximum temperatures measured near each of the four Feshbach resonances, as recorded in Fig. S4. Even for the maximum temperature increase (60 %) encountered for the "on-resonance" value near 9 G, the expected correction is less than 20 %, and we stress that this is the worst case scenario; at all other magnetic fields and all earlier times the temperature increase is smaller, and thus the change in coupling factor is less pronounced. We conclude that the (approximate) conversion to atomic population  $N_2$  from our dispersive signal  $A$ , based on a value for  $C_2$  calibrated at a temperature of  $T = 1.4 \mu\text{K}$ , is reasonable within our experimental setting.

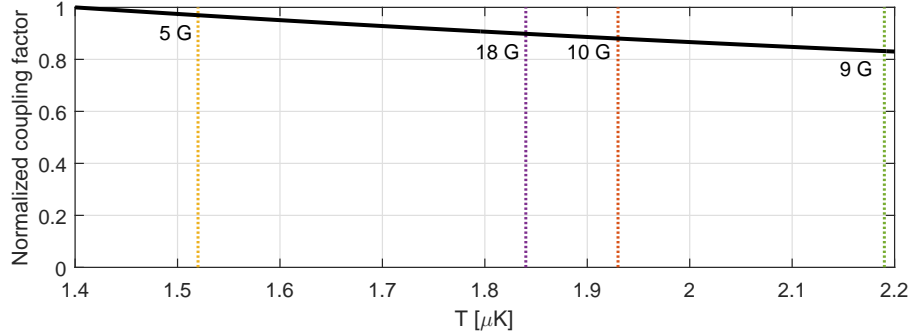


FIG. S6. (Color online) Variation of geometric coupling factor with temperature, across the full temperature range of the samples in this work (solid line). The dotted lines indicate the maximum final temperatures measured for each of the four Feshbach resonances.

## S.V. SWEEPING RANGE IN FEWER STEPS

Background losses in the sample limit the total duration of each magnetic field sweep or hold time. The atomic density of the cloud reduces by 40 % over a 200 ms period even in the absence of Feshbach interactions, making density-dependent Feshbach loss more difficult to detect. In the main text, we required 21 consecutive sweeps of 200 ms duration to cover the full >18 G

magnetic field range at a low enough rate to dispersively detect losses due to the weak  $\simeq 5$  G resonance. If we are only interested in stronger features however, we can increase the sweep rate significantly. An example data set is shown in Fig. S7 where we used just 6 sweeps, each 2.9 G wide, to cover a 16 G range. Shaded gray regions indicate where we expect to see Feshbach resonances, based on our investigation in the main text. Steps in the signal are evident at the  $\simeq 18$  G,  $\simeq 10$  G and  $\simeq 9$  G Feshbach resonances, but there is no clear evidence of loss near 5 G.

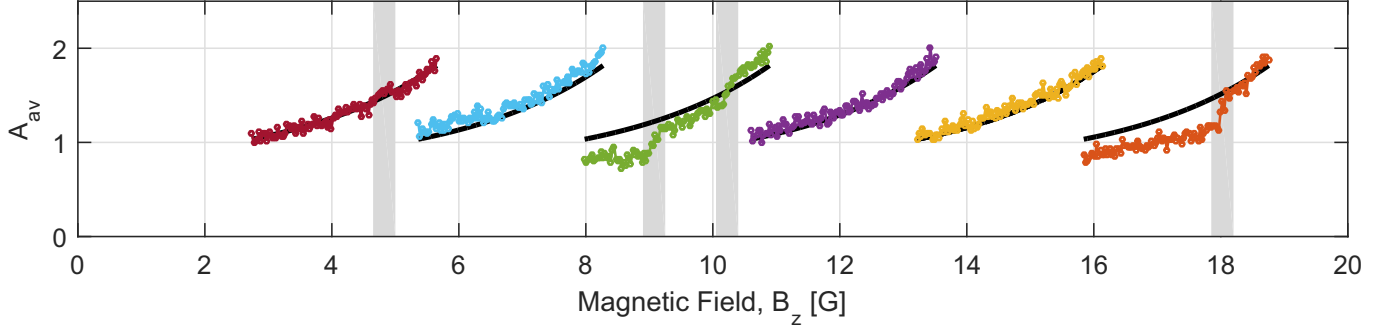


FIG. S7. (Color online) Dispersive signal ( $A_{av}$ , averaged over three experimental runs) recorded during six overlapping magnetic field sweeps. The black line indicates a reference data set, and shaded gray boxes indicate regions in which we know there is a Feshbach resonance.

- 
- [S1] P. van der Straten and H. Metcalf, *Atoms and molecules interacting with light*, 1st ed. (Cambridge University Press, 2016).  
 [S2] C. Chin, R. Grimm, P. Julienne, and E. Tiesinga, [Rev. Mod. Phys. \*\*82\*\*, 1225 \(2010\)](#).  
 [S3] Q. Beaufils, A. Crubellier, T. Zanon, et al., [Phys. Rev. A \*\*79\*\*, 032706 \(2009\)](#).  
 [S4] C. Ticknor, C. A. Regal, D. S. Jin, and J. L. Bohn, [Phys. Rev. A \*\*69\*\*, 042712 \(2004\)](#).